Current-induced spin polarization in Janus WSSe monolayer

Sheng-Bin Yu [1,2,*] Shu-Han Sun,[1,2,*] Ma Zhou,[3] Dong Zhang [1,2,*,†] and Kai Chang[1,2,‡]

[1]*SKLSM, Institute of Semiconductors, Chinese Academy of Sciences, P.O. Box 912, Beijing 100083, China*
[2]*College of Materials Science and Opto-Electronic Technology, University of Chinese Academy of Sciences, Beijing 100049, China*
[3]*Department of Physics, Nanchang University, Nanchang 330031, China*

Janus engineering of transition metal dichalcogenide monolayers breaks the vertical mirror symmetry and induces huge built-in polarization and large Rashba spin-orbit coupling. By performing first-principles calculations, we find that the Rashba spin-orbit coupling induces sizable current-induced spin polarization in both the conduction and valence bands in the Janus WSSe monolayer, which is comparable to that in perovskite oxide interfaces. By constructing the low-energy $\mathbf{k} \cdot \mathbf{p}$ Hamiltonian from the invariant theory, we find a sign change of the current-spin conductivity at chemical potential $\mu \approx -0.73$ eV, which indicates the flip of spin polarization and is attributed to the competition between the intrinsic Rashba spin-orbit coupling and the hexagonal warping of the valence bands. Our numerical and analytic results suggest that the current-induced spin polarization in the Janus WSSe monolayer is insensitive to temperature and impurity concentration but can be effectively tuned by external biaxial or uniaxial strain. The Janus WSSe monolayer could be a promising candidate to realize flexible two-dimensional spintronics devices.

I. INTRODUCTION

Transition metal dichalcogenide (TMD) monolayers, an emerging class of two-dimensional (2D) semiconductors possessing direct band gaps as well as multiple degrees of freedom, such as charge, valley, and spin, have attracted intensive investigations in both novel physical phenomena and versatile potential applications in nanoelectronics, valleytronics, and optoelectronics [1–5]. Usually, electrical control of electron spin in TMD-based spintronic devices via the Rashba spin-orbital coupling (SOC) is required. The efficient utilization of Rashba SOC in pristine TMD monolayers usually requires strong external electric fields using the ionic gate technique [6–8]. Recently, by substituting one sublayer of chalcogen atoms with another element completely, Janus MoSSe [9–11] and WSSe [12–14] monolayers have been successfully synthesized. Compared with their pristine counterparts, the Janus TMD monolayers lack both in-plane inversion symmetry and out-of-plane mirror symmetry. Furthermore, a huge vertical built-in polarization emerges, because of the difference between electronegativities of upper and lower *M-X* (chalcogenide atom) bonds. Therefore the Janus TMD monolayers offer a new set of properties including piezoelectricity [15], enhanced photocatalysis [16], tunable transport properties [17], long exciton lifetimes [18], and large Rashba SOC splitting [19]. In our previous work, we have demonstrated a considerable intrinsic spin Hall effect enhanced by Rashba SOC in the Janus MoSSe monolayer, which implies that the Janus TMD monolayers could be suitable candidates in flexible 2D spintronics applications [20].

The essence of spintronics without ferromagnetic materials relies on the SOC-induced interconversions between spin and charge [21–28]. In addition to the spin Hall effect, the inverse spin-galvanic effect [29–33], which describes the current-induced spin polarization (CISP), offers us another efficient way to generate nonequilibrium spin polarization electrically. In the presence of Rashba SOC, considering two-dimensional systems' lack of inversion symmetry, persistent charge current produces a steady nonequilibrium spin polarization perpendicular to the applied bias. As shown in Fig. 1(a), a shift of the Fermi surface in the direction of the persistent current (j_x) induces an overpopulation of spins along the direction $-y$, because of the spin-momentum locking feature of the Rashba SOC. Therefore the nonferromagnetic system possesses a spin-polarized charge current [29–33]. The CISP have been experimentally verified in series of systems, such as a nonmagnetic TMD-graphene heterostructure [34], Be_2Se_3 films, and a two-dimensional electron gas (2DEG) at the InAs(001) interface [35,36]. Theoretically, tunable nonequilibrium spin polarization has been proposed in an InSe monolayer in the presence of a perpendicular electric field, for the induced Rashba SOC [37].

In this paper, we focus on the CISP in the recently synthesized Janus WSSe monolayer, and this paper is organized as follows: In Sec. II, we present the $\mathbf{k} \cdot \mathbf{p}$ Hamiltonian based on the invariant theory and the formulas to compute the spin-charge conductivity, as well as computational details of the numerical first-principles calculations about the Janus monolayer. In Sec. III, we present the intrinsic current-induced spin polarization of monolayer Janus WSSe based on both numerical results and $\mathbf{k} \cdot \mathbf{p}$ Hamiltonian analyses. The effects

*These authors contributed equally to this work.
†Corresponding author: zhangdong@semi.ac.cn
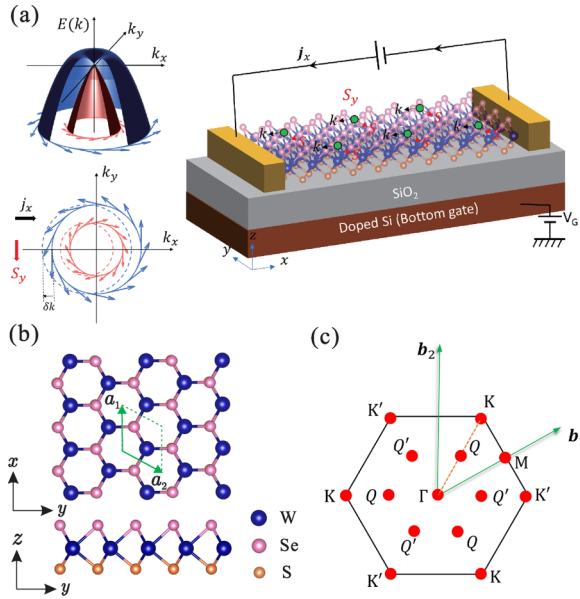‡Corresponding author: kchang@semi.ac.cn

FIG. 1. (a) Schematics of the CISP effect and the experimental setup. The left panels show typical Rashba splitting bands and longitudinal spin polarization induced by transversal charge current, because of the shift of the Fermi surface. In the right panel, the transversal charge current is applied between brown contacts and along the x direction. The bottom gate V_G is used to adjust the chemical potential of the Janus WSSe monolayer. (b) Top and side views of the Janus WSSe monolayer. The hexagonal primitive cell (defined by a_1 and a_2) is indicated by the dashed lines, and the tungsten atoms, sulfur atoms, and selenium atoms are illustrated with blue, orange, and pink spheres, respectively. (c) The first Brillouin zone of the hexagonal primitive cell (defined by b_1 and b_2); the high-symmetry points are labeled with red dots.

of temperature and disorders are discussed. Of particular importance, external strains as effective means of modulation are demonstrated. In Sec. IV, we summarize this work with a brief conclusion.

II. MODEL AND THEORY

A. Janus WSSe monolayer and the CISP

The crystal structure of the Janus WSSe monolayer is illustrated in Fig. 1(b). Similar to the WS_2 and WSe_2 monolayers, in the Janus WSSe monolayer, each W atom is bonded with the six nearest chalcogen atoms, and this forms a honeycomb structure in the x-y plane [top view in Fig. 1(b)]. Vertically, the W sublayer is sandwiched by heterogeneous S and Se sublayers, instead of homogeneous S or Se sublayers [side view in Fig. 1(b)]. Due to the slightly difference between the bond lengths of W-S and W-Se, the point group changes from D_{3h} to C_{3v}. The equilibrium lattice constants are calculated to be $a_1 = a_2 \approx 3.25$ Å. The prototype experimental setup to detect the CISP is given in Fig. 1(a). J_x is the steady charge current driven by electric field E_x along the Janus WSSe monolayer, and S_y is the expected steady nonequilibrium spin polarization of conduction electrons, induced by Rashba SOC in the Janus WSSe monolayer.

TABLE I. Character table of the point group C_{3v} and basis functions for each irreducible representation. Here, (x, y, z) are the three Cartesian components of an ordinary vector (which changes sign under spatial inversion) and (R_x, R_y, R_z) are the three Cartesian components of an axial vector (which remains invariant under spatial inversion).

C_{3v}	E	$2C_3$	$3\sigma_v$	Basis functions
Γ_1	1	1	1	z
Γ_2	1	1	-1	R_z
Γ_3	2	-1	0	(x, y) (R_x, R_y)

Usually, proper definition of the pure spin current is important in the spin Hall effect [38]. However, the CISP effect describes the homogenous spin-polarized charge current. In order to understand the underlying physics, we ignore the local band bending near the Janus monolayer and contacts and focus on the homogenous spin-polarized charge current only. Therefore, without loss of generality, the CISP is defined by the proportionality $S_\beta = \sigma_{\beta\alpha}^{\text{C-S}} E_\alpha$. According to the Onsager relation, the charge-to-spin (C-S) conductivity is equal to the spin-to-charge (S-C) conductivity, which reads [39,40]

$$\sigma_{\beta\alpha}^{\text{C-S}}(\mu) = -\frac{1}{2\pi} \int \frac{d^2\mathbf{k}}{(2\pi)^2} \text{Tr}\big[s_\beta G_{\mathbf{k}}^R(\mu) J_\alpha G_{\mathbf{k}}^A(\mu) \big], \quad (1)$$

where $J_\alpha = ev_\alpha = \frac{e}{\hbar} \frac{\partial \mathcal{H}}{\partial k_\alpha}$ is the charge current operator, $s_\beta = \frac{\hbar}{2}\sigma_\beta$ is the spin operator, and $G_{\mathbf{k}}^{R(A)}(\mu)$ is the retarded (advanced) Green's function corresponding to the unperturbed Hamiltonian $\mathcal{H}$ of the system at the chemical potential μ. In the limit of a clean system, the C-S conductivity $\sigma_{\beta\alpha}^{\text{C-S}}$ would become infinite. However, in real materials, due to the unavoidable impurity scattering, the lifetime of the conducting electrons is finite.

B. Effective Hamiltonian

The key to calculate the C-S conductivity is to obtain an effective Hamiltonian describing the band structures of the Janus WSSe monolayer properly. In this paper, we get the effective Hamiltonian both numerically and analytically.

1. $\mathbf{k} \cdot \mathbf{p}$ Hamiltonian

For a better understanding of the underlying physics, invariant theory [41–43] is used to construct the $\mathbf{k} \cdot \mathbf{p}$ Hamiltonian of the Janus WSSe monolayer near the high-symmetry points. The $\mathbf{k} \cdot \mathbf{p}$ Hamiltonian can be derived from the invariants in the Brillouin zone of given point group and time-reversal operator.

a. $\mathbf{k} \cdot \mathbf{p}$ Hamiltonian at the Γ point. The symmetry group of the Janus WSSe monolayer is C_{3v} and $\hat{T}$, with the following generators: (i) an identity operator E, (ii) a threefold rotation operator C_3, (iii) a mirror reflection operator σ_v, and (iv) a time-reversal operator $\hat{T}$. Their irreducible representations and corresponding basis functions are listed in Table I. The top valence band at the Γ point belongs to Γ_1, and the invariants up to $O(k^3)$ for the $\mathbf{k} \cdot \mathbf{p}$ Hamiltonian are obtained and shown in Table II. In addition, since the Hamiltonian should remain invariant under the time-reversal operation $\hat{T}$,

TABLE II. Invariants belonging to C_{3v} constructed from the 2D momentum operator (k_x, k_y) up to the third order and/or spin operator (s_x, s_y, s_z). Here, $k^2 \equiv k_x^2 + k_y^2$. However, $(k_y^2 - k_x^2)s_y + 2k_xk_ys_x$ is not invariant under time reversal.

	Invariants
First order	$k_xs_y - k_ys_x$
Second order	k^2
Third order	$(k_y^2 - k_x^2)s_y + 2k_xk_ys_x$
	$(k_x^3 - 3k_xk_y^2)s_z$

the second-order term, $(k_y^2 - k_x^2)s_y + 2k_xk_ys_x$ in Table II, is not allowed.

Therefore a third-order $\mathbf{k} \cdot \mathbf{p}$ Hamiltonian $H_{\mathbf{k} \cdot \mathbf{p}}^{\Gamma}$ at the Γ point satisfying both the crystal and time-reversal symmetry reads

$$H_{\mathbf{k} \cdot \mathbf{p}}^{\Gamma}(\mathbf{k}) = \frac{k^2}{2m^*} + \alpha(k_xs_y - k_ys_x) + \gamma(k_x^3 - 3k_xk_y^2)s_z, \quad (2)$$

where m^* denotes the effective mass. The second term, H_R^{Γ}, describes Rashba SOC. The last term, H_w^{Γ}, is the so-called hexagonal warping term and is responsible for the hexagonal distortions of the original concentric circular Fermi loops [44]. The strength of hexagonal warping is determined by the parameter γ. It is notable that H_w^{Γ} vanishes along the Γ-M direction, because s_z is odd under this mirror-symmetric operation, and it reaches a maximum along the direction Γ-K. The band dispersion of $H_{\mathbf{k} \cdot \mathbf{p}}^{\Gamma}$ is

$$E_{\pm}^{\Gamma}(\mathbf{k}) = \frac{k^2}{2m^*} \pm \sqrt{\alpha^2 k^2 + \gamma^2 k_x^2 (k_x^2 - 3k_y^2)^2}, \quad (3)$$

where $E_{\pm}$ denotes the eigenvalue of the upper or lower energy band.

b. $\mathbf{k} \cdot \mathbf{p}$ *Hamiltonian at the K and K' points.* For the TMD monolayer family, usually the K and K' points are of particular importance. At the K and K' points, the σ_v operation is absent, and the point group changes from C_{3v} to C_3. Their irreducible representations and the corresponding basis functions of C_3 are listed in Table III. The valence band maximum (VBM) and conduction band minimum (CBM) belong to K_1 and K_3, respectively.

All the invariants up to $O(k^2)$ for the $\mathbf{k} \cdot \mathbf{p}$ Hamiltonian are obtained and shown in Table IV. In the basis of $|v\rangle$ and $|c\rangle$, the $\mathbf{k} \cdot \mathbf{p}$ Hamiltonian without SOC at the K and K' points can

TABLE III. Character table of the point group C_3 and basis functions for each irreducible representation. Here, (x, y, z) are the three Cartesian components of an ordinary vector (which changes sign under spatial inversion) and (R_x, R_y, R_z) are the three Cartesian components of an axial vector (which remains invariant under spatial inversion).

C_3	E	C_3	C_3^2	Basis functions
K_1	1	1	1	z; R_z
K_2	1	$e^{2i\pi/3}$	$e^{-2i\pi/3}$	$x + iy$; $R_x + iR_y$
K_3	1	$e^{-2i\pi/3}$	$e^{2i\pi/3}$	$x - iy$; $R_x - iR_y$

TABLE IV. Invariants belonging to C_3 constructed from the 2D momentum operator (k_x, k_y) up to the second order and/or spin operator (s_x, s_y, s_z). Here, $k^2 \equiv k_x^2 + k_y^2$.

H^{K_1, K_1}	H^{K_3, K_3}	H^{K_1, K_3}
s_z		$s_y - is_x$
$k_xs_y - k_ys_x$		$k_y - ik_x$
k^2		$(k_y - ik_x)s_z$
$(k_x^2 - k_y^2)s_y - 2k_xk_ys_x$		$k_x^2 - k_y^2 + 2ik_xk_y$
k^2s_z		$(k_x^2 - k_y^2 + 2ik_xk_y)s_z$
		$k^2(s_y - is_x)$

be written as

$$H^{K/K'}(\mathbf{k}) = \begin{pmatrix} H_{vv}^{K/K'} & H_{vc}^{K/K'} \\ (H_{vc}^{K/K'})^* & H_{cc}^{K/K'} \end{pmatrix}, \quad (4)$$

where

$$H_{vv}^{K/K'} = E_v + C_vk^2,$$
$$H_{vc}^{K/K'} = A_{vc}(\nu k_y - ik_x) + B_{vc}(k_x^2 - k_y^2 + 2\nu ik_xk_y), \quad (5)$$
$$H_{cc}^{K/K'} = E_c + C_ck^2,$$

where E_v and E_c are band-edge energies of the valence band and conduction band, respectively. C_v, C_c, A_{vc}, and B_{vc} are four parameters which can be quantitatively determined by comparing the band structures obtained from the $\mathbf{k} \cdot \mathbf{p}$ Hamiltonian with the first-principles calculations without SOC in the vicinity of the K and K' points as listed in Table V, and $\nu = \pm 1$ is the valley index. By using the spin-dependent invariants, we can construct the spin-related term

$$H_{soc}^{K/K'}(\mathbf{k}) = \begin{pmatrix} H_{vv,soc}^{K/K'} & H_{vc,soc}^{K/K'} \\ (H_{vc,soc}^{K/K'})^* & H_{cc,soc}^{K/K'} \end{pmatrix}, \quad (6)$$

where

$$H_{vv,soc}^{K/K'} = \nu\lambda_{vv}s_z + \nu\alpha_{vv}(k_xs_y - k_ys_x)$$
$$+ \nu\beta_{vv}[(k_x^2 - k_y^2)s_x - 2k_xk_ys_y] + \nu\xi_{vv}k^2s_z,$$
$$H_{cc,soc}^{K/K'} = \nu\lambda_{cc}s_z + \nu\alpha_{cc}(k_xs_y - k_ys_x)$$
$$+ \nu\beta_{cc}[(k_x^2 - k_y^2)s_x - 2k_xk_ys_y] + \nu\xi_{cc}k^2s_z, \quad (7)$$
$$H_{vc,soc}^{K/K'} = \nu\lambda_{vc}(s_y - is_x) + \nu\alpha_{vc}(k_y - ik_x)s_z$$
$$+ \beta_{vc}[\nu(k_x^2 - k_y^2) + 2ik_xk_y]s_z + \nu\xi_{vc}k^2(s_y - is_x),$$

which contains 12 new parameters describing SOC, namely, λ_{vv}, λ_{cc}, λ_{vc}, α_{vv}, α_{cc}, α_{vc}, β_{vv}, β_{cc}, β_{vc}, ξ_{vv}, ξ_{cc}, and ξ_{vc}. The total Hamiltonian is $H_{\mathbf{k} \cdot \mathbf{p}}^{K/K'} = H^{K/K'} + H_{soc}^{K/K'}$. The new parameters can be determined by fitting the band structures obtained from the $\mathbf{k} \cdot \mathbf{p}$ Hamiltonian with first-principles calculations including the SOC effect as listed in Table V.

2. Tight-binding model

A Wannier tight-binding (WTB) model [45,46] of the Janus WSSe monolayer is derived from accurate first-principles calculation, using the WANNIER90 software package

TABLE V. The parameters of the $\mathbf{k} \cdot \mathbf{p}$ Hamiltonians $H_{\mathbf{k} \cdot \mathbf{p}}^{\Gamma}$ and $H_{\mathbf{k} \cdot \mathbf{p}}^{K/K'}$ in the Janus WSSe monolayer.

Parameter	Value	Unit	Parameter	Value	Unit	Parameter	Value	Unit
m^*	−2.49	m_e	α	0.1136	eV Å	γ	−0.9617	eV Å^3
E_v	−0.4628	eV	E_c	−0.2292	eV	A_{vc}	3.3658	eV Å
B_{vc}	−1.5010	eV Å^2	C_v	−1.9853	eV Å^2	C_c	3.9544	eV Å^2
λ_{vv}	0.2122	eV	λ_{cc}	0.0318	eV	λ_{vc}	0.0018	eV
α_{vv}	0.9890	eV Å	α_{cc}	0.3187	eV Å	α_{vc}	0.1438	eV Å
β_{vv}	0.6947	eV Å^2	β_{cc}	0.7873	eV Å^2	β_{vc}	0.9268	eV Å^2
ξ_{vv}	−1.6211	eV Å^2	ξ_{cc}	−3.4257	eV Å^2	ξ_{vc}	0.0581	eV Å^2

[47]. The corresponding matrix Hamiltonian can be written as

$$\mathcal{H}^{ij}(\mathbf{k}) = \sum_{\mathbf{R}} H^{ij}[\mathbf{R}] e^{i\mathbf{k} \cdot (\mathbf{R} + \mathbf{t}_j - \mathbf{t}_i)}, \qquad (8)$$

where $H^{ij}[\mathbf{R}]$ is the hopping term between the jth orbit in the unit cell at location $\mathbf{R}$ and the ith orbital in the home orbital in the home unit cell $\mathbf{R} = 0$ and indices i, j include the spin index for simplicity. The WTB Hamiltonian utilizes maximally localized Wannier functions (MLWFs) [48,49] as basis orbitals to capture the physics of the system. In order to construct the MLWFs, the converged total Wannier spread is less than 10^{-10} Å^2 in our calculations.

C. First-principles calculations

The first-principles calculations are performed with the Vienna *ab initio* simulation package (VASP) code [50,51] based on density functional theory (DFT) [52,53]. The freestanding Janus WSSe monolayer is placed in the x-y plane with a vacuum slab of 20 Å thickness in the z direction to avoid unphysical interactions between periodic adjacent slabs. The projector augmented wave (PAW) [54] pseudopotential with exchange-correlation functional under the generalized gradient approximation (GGA) of Perdew, Burke, and Ernzerhof (PBE) [55] is used in our calculations. The equilibrium crystal structure is obtained by full atomic relaxation with the maximum force on each atom less than 0.01 eV/Å, and the convergence criterion of the total energy is set to 10^{-10} eV. The first Brillouin zone (FBZ) is sampled in $9 \times 9 \times 1$ Γ-centered k-point meshes for lattice structure optimization and $16 \times 16 \times 1$ for the calculation of electronic properties. A plane-wave cutoff energy is set to 500 eV, and the Gaussian smearing method with a width of 0.01 eV is employed. The SOC effect is included in all the calculations as well as the construction of the WTB Hamiltonian.

III. RESULTS AND DISCUSSION

The band structures and projected density of states (DOS) of the Janus WSSe monolayer are shown in Fig. 2. From the band structures, one can find a direct band gap $E_g = 1.43$ eV between the conduction band minimum (CBM) and the valence band maximum (VBM) locating at the K and K' points in the FBZ. As shown in Fig. 2(b), the major components of the VBM and CBM are d orbitals of W atoms; more specific information is included in the d-orbital-resolved projected band structures as shown in Fig. 2(a). The VBM locates at the K and K' points, with sizable Zeeman-like SOC splitting,

and the major components are $d_{x^2+y^2}$ and d_{xy} orbitals of the W atoms. The CBM locates at the K and K' points as well, but the major component is the d_{z^2} orbital of W atoms. Meanwhile the second conduction band minimum, denoted as the Q and Q' points, is composed of the d_{xz} and d_{yz} orbitals. It is noteworthy that a large Rashba SOC emerges at the Γ point of the valence bands, which is dominated by the d_{z^2} orbital component and stems from the large built-in electric field in the Janus WSSe monolayer, similar to the case in the Janus MoSSe monolayer [20].

Considering an ideal clean system, the carrier lifetime $\tau \to +\infty$ and the C-S conductivity $\sigma_{\beta\alpha}^{\text{C-S}}$ diverge as $\sigma_{\beta\alpha}^{\text{C-S}} = D_{\beta\alpha}^{\text{C-S}} \tau$. Then the Drude-like coefficient of the C-S conversion can be written as [56]

$$D_{\beta\alpha}^{\text{C-S}} = \sum_{m \neq n} \int \frac{d^2\mathbf{k}}{(2\pi)^2} [f(E_{m,\mathbf{k}}) - f(E_{n,\mathbf{k}})] \mathbf{P}(\mathbf{k}), \qquad (9)$$

where

$$\mathbf{P}(\mathbf{k}) = -\pi \cdot \text{Re} \frac{\langle m, \mathbf{k} | s_\beta | n, \mathbf{k} \rangle \langle n, \mathbf{k} | J_\alpha | m, \mathbf{k} \rangle}{E_{m,\mathbf{k}} - E_{n,\mathbf{k}} + i0^+}. \qquad (10)$$

$f(E) = 1/(e^{(E-\mu)/(k_B T)} + 1)$ is the Fermi-Dirac distribution. $E_{m(n),\mathbf{k}}$ is the energy at the $\mathbf{k}$ point, and $|m(n), \mathbf{k}\rangle$ is the corresponding wave function. It is notable that the chemical potential μ is an adjustable parameter which can be tuned by
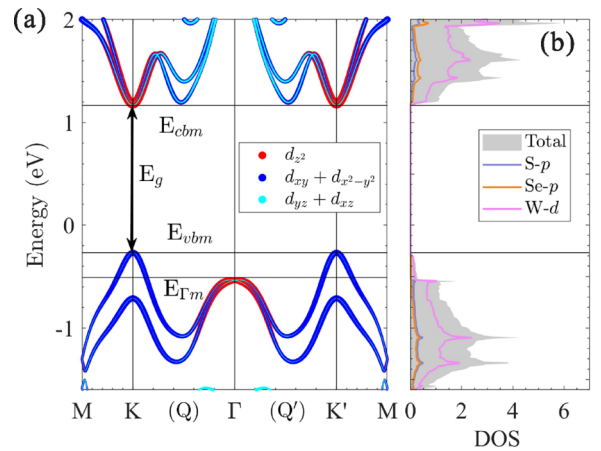

FIG. 2. (a) The band structures of the Janus WSSe monolayer. The d orbitals of W atoms are decomposed into d_{z^2}, $d_{x^2-y^2} + d_{xy}$ and $d_{xz} + d_{yz}$ components and are indicated by red-, blue-, and cyan-colored dots, respectively. (b) The decomposed density of states (DOS) of p orbitals of S and Se atoms as well as d orbitals of W atoms of the Janus WSSe monolayer.
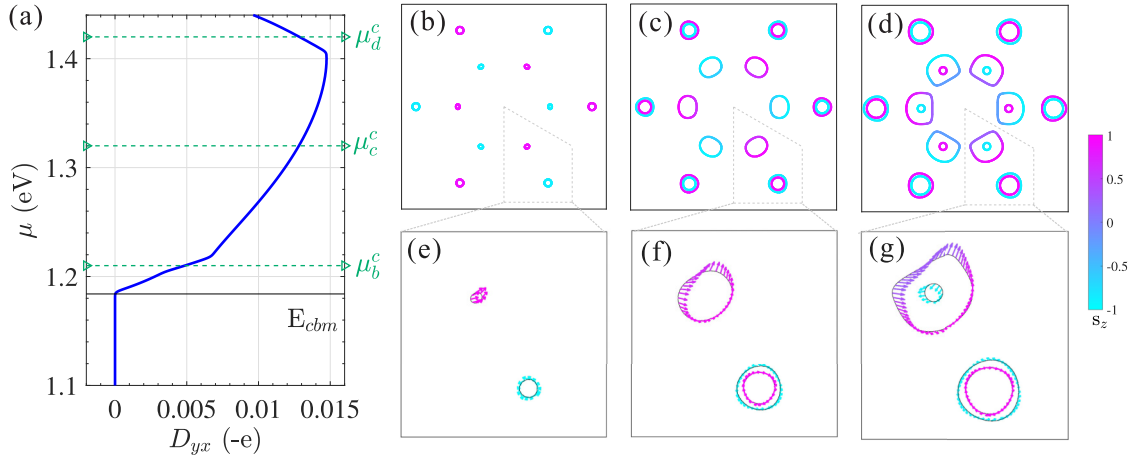
FIG. 3. (a) The C-S response D_{yx} of the Janus WSSe monolayer in the vicinity of the conduction band minimum and at the temperature $T = 10$ K. (b), (c), and (d) show the spin textures at chemical potentials of $\mu = \mu_b^v$, μ_c^v, and μ_d^v, respectively. The chemical potentials are indicated with green dashed horizontal lines in (a), accordingly. (e), (f), and (g), The zoomed-in spin textures of areas in the gray dashed boxes in (b), (c), and (d), respectively. The two spin textures locate at the Q and K points as shown in Fig. 1(c). The magnitudes of the out-of-plane spin component s_z agree with the color bar on the right.

gate voltage and, in the formula $D_{yx}^{C\text{-}S} = -D_{xy}^{C\text{-}S}$, is restricted by the C_{3v} symmetry of the Janus WSSe monolayer. At zero temperature, the integral over the FBZ in Eq. (9) is limited within a small region where $E_{m,\mathbf{k}} < \mu < E_{n,\mathbf{k}}$ ($m < n$).

Figure 3(a) shows the Drude-like coefficient $D_{yx}^{C\text{-}S}$ as a function of chemical potential μ in the conduction bands. By adjusting the chemical potential smoothly upwards, there are two remarkable features. Firstly, from the spin texture, one can find that, compared with the spin textures in the valence band, the spins in the vicinity of the K and K' points in the conduction band tend to lie on the S_x-S_y plane, which we attribute to the larger Drude-like coefficient $D_{yx}^{C\text{-}S}$ with respect to that in the valence band. Moreover, due to the energy position of the Q (Q') valley locating very close to the K (K') point [see Fig. 2(a)], the contribution to $D_{yx}^{C\text{-}S}$ that comes from the Q (Q') point increases as the chemical potential shifts as shown in Figs. 3(c) and 3(d). For clarity, a pair of zoomed-in spin textures around the Q and K points are shown in Figs. 3(f) and 3(g)], and the corresponding chemical potentials are indicated with green dashed lines in Fig. 3(a). The two features lead to two obvious discontinuity points of $D_{yx}^{C\text{-}S}$ in Fig. 3(a) with $\mu \approx 1.22$ eV and $\mu \approx 1.41$ eV, respectively.

Likewise, Fig. 4(a) shows the Drude-like coefficient $D_{yx}^{C\text{-}S}$ as a function of chemical potential μ in the valence bands. The curve of $D_{yx}^{C\text{-}S}$ starts at the edge of the band gap with a very small negative value, which refers to the topmost valence band at the K and K' points. The corresponding spin textures [Fig. 4(b)] reveal that $D_{yx}^{C\text{-}S}$ is attributed to six Fermi pockets with alternative positive and negative s_z components. It is worth emphasizing that in the range $E_{\Gamma m} < \mu < E_{vbm}$ the vertical alignment of spin orientations is the result of the Zeeman-like SOC at the K and K' points in the valence band. However, in the presence of Rashba SOC, all the spins are tilted, and the net nonzero in-plane spin components (s_x, s_y) lead to the nonzero value of $D_{yx}^{C\text{-}S}$.

As the chemical potential shifts downwards continuously, a peak of $D_{yx}^{C\text{-}S}$ occurs at $\mu = E_{\Gamma m}$, where the contribution from
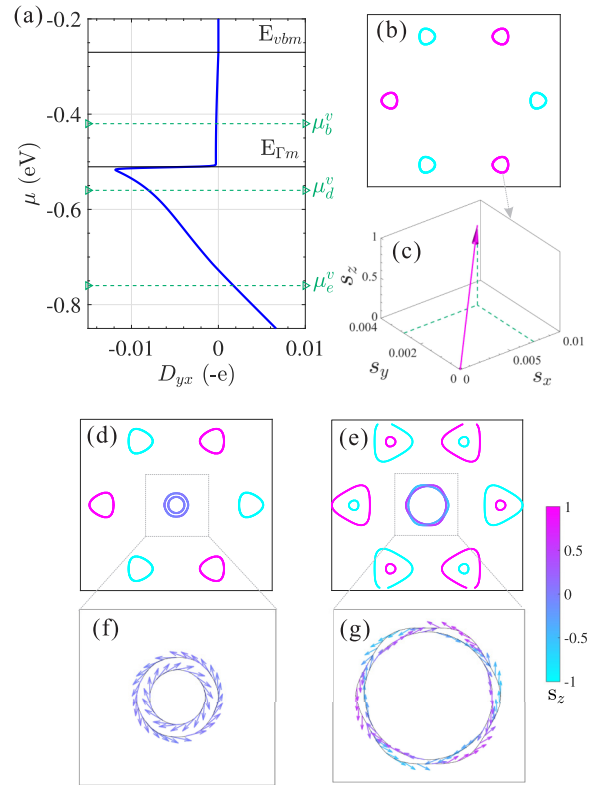

FIG. 4. (a) The C-S response D_{yx} of the Janus WSSe monolayer in the vicinity of the valence band maximum in the clean limit and at the temperature $T = 10$ K. (b), (d), and (e) show the spin textures at chemical potentials of $\mu = \mu_b^v$, μ_d^v, and μ_e^v, respectively. The chemical potentials are indicated with green dashed horizontal lines in (a), accordingly. (c) Spatial spin orientation of points near the K point [as indicated by the gray arrow in (b)]; the major component is aligned to the s_z. (f) and (g) are zoomed-in spin textures of areas in the gray dashed boxes in (d) and (e) at the Γ point, respectively. The magnitudes of the out-of-plane spin component s_z agree with the color bar on the right.

spin textures at the Γ point takes part and becomes dominant rapidly. In Fig. 4(d), one can find a pair of concentric circles with opposite in-plane spin orientations [zoomed-in view shown in Fig. 4(f)] in the center of the FBZ, except for the six Fermi pockets on the corners. This pair of concentric circles are the fingerprint of Rashba SOC, which can be described by a 2×2 effective $\mathbf{k} \cdot \mathbf{p}$ Hamiltonian, $H_R = \alpha(k_x s_y - k_y s_x)$, where α denotes the so-called Rashba parameter. At equilibrium, for a given momentum, opposite spins cancel in pairs with the same magnitude, and in the presence of an applied electric field, additional momentum is added along the y direction, which induces nonzero net spin by summing the k_x and $-k_x$ states, as well as net spin polarization. This is the typical CISP in the literature, and the spin polarization is linearly proportional to the Rashba parameter α. From the numerical results, one can find that the value of $D_{yx}^{\text{C-S}}$ has the same order of magnitude as that in the $LaAlO_3/SrTiO_3$ (LAO/STO) oxide interface [about -0.01 $(-e)$] [56], due to the large intrinsic Rashba SOC in the Janus WSSe monolayer.

Unexpectedly, as the chemical potential goes deep into the valence band, and the Drude-like coefficient $D_{yx}^{\text{C-S}}$ increases gradually and eventually reverses sign at chemical potential $\mu \approx -0.73$ eV. To capture the underlying physics of the sign change, spin textures at $\mu = \mu_e^v$ are depicted in Figs. 4(e) and 4(g). One can find that the two concentric circles endure dramatic deformation into two hexagons. Furthermore, unlike the zero s_z components on the concentric circles, s_z oscillates periodically on the hexagons, and the in-plane spin orientations are not strictly tangent to the hexagonal contour.

The phenomenological description of sign change is not adequate. In order to capture the underlying physics of sign change of CISP, we focus on the effective $\mathbf{k} \cdot \mathbf{p}$ Hamiltonian. For the valence band, since the dominant components of the Drude-like coefficient $D_{yx}^{\text{C-S}}$ are attributed to states in the vicinity of the Γ point, we consider the irreducible representation of Γ_1, whose orbital wave function remains invariant under all operations of C_{3v}. As shown in Fig. 5(a), the obtained parameters of Hamiltonian $H_{\mathbf{k} \cdot \mathbf{p}}^{\Gamma}$ are $m^* = -2.49$ m_e, $\alpha = 113.6$ meV Å, and $\gamma = -961.7$ meV Å³. Although the Hamiltonian $H_{\mathbf{k} \cdot \mathbf{p}}^{\Gamma}$ is threefold invariant, the hexagonal warping of the Fermi surface is sixfold symmetric under time-reversal symmetry. The corresponding spin texture at the chemical potential $\mu = \mu_e^v$ calculated from the Hamiltonian $H_{\mathbf{k} \cdot \mathbf{p}}^{\Gamma}$ [see Fig. 5(b)] is consistent with the previous first-principles calculations [see Fig. 4(g)].

The Drude-like coefficient $D_{yx}^{\text{C-S}}$ derived from the $\mathbf{k} \cdot \mathbf{p}$ Hamiltonian $H_{\mathbf{k} \cdot \mathbf{p}}^{\Gamma}$ is shown in Fig. 5(c). In the region between $E_{\Gamma m}$ and E_{vbm}, D_{yx} vanishes, which fits the nonzero D_{yx} obtained from the first-principles calculations. More importantly, when the chemical potential decreases ($\mu < E_{\Gamma m}$), $D_{yx}^{\text{C-S}}$ derived from the $\mathbf{k} \cdot \mathbf{p}$ Hamiltonian endures a gradual increase and eventually reverses sign at chemical potential $\mu \approx -0.81$ eV, which is qualitatively close to the results of first-principles calculations. In order to interpret the sign change process, the integrated $\mathbf{P}(\mathbf{k})$ in Eq. (10) is divided into two parts (unit is $-e$),

$$\mathbf{P}_1(\mathbf{k}) = \frac{\pi}{2} \frac{-\alpha^3 k_y^2}{\left[\alpha^2 k^2 + \gamma^2 k_x^2 \left(k_x^2 - 3k_y^2 \right)^2 \right]^{\frac{3}{2}}},$$
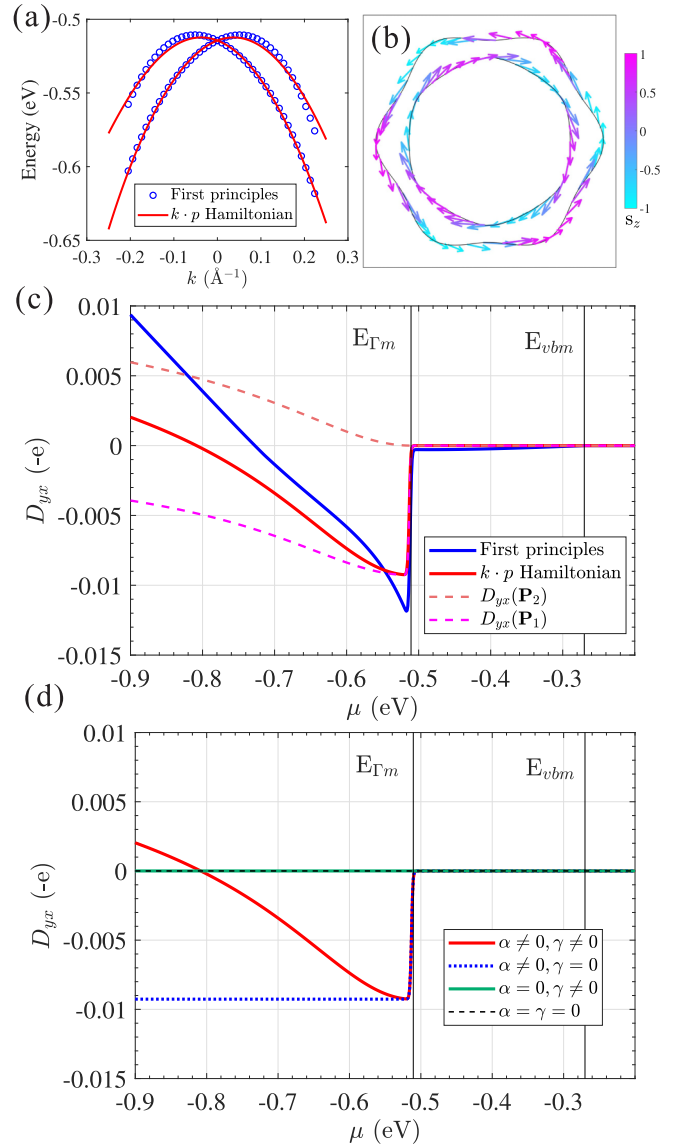
FIG. 5. (a) The band structures of the Janus WSSe monolayer in the vicinity of the Γ point obtained by the $\mathbf{k} \cdot \mathbf{p}$ Hamiltonian (red solid lines) and first-principles calculations (blue open circles). (b) The spin textures at the chemical potential $\mu = \mu_e^v$ in Fig. 4 obtained by the $\mathbf{k} \cdot \mathbf{p}$ Hamiltonian. (c) The C-S response D_{yx} of the Janus WSSe monolayer obtained by the $\mathbf{k} \cdot \mathbf{p}$ Hamiltonian (red solid line) and first-principles calculations (blue solid line) in the clean limit and at the temperature $T = 10$ K. $D_{yx}(\mathbf{P}_1)$ and $D_{yx}(\mathbf{P}_2)$ are the integrations of $\mathbf{P}_1$ and $\mathbf{P}_2$, respectively. (d) Comparison of the C-S response D_{yx} of the Janus WSSe monolayer obtained by the $\mathbf{k} \cdot \mathbf{p}$ Hamiltonian (red solid line) and the same Hamiltonian but with $\alpha = 0$ (green solid line), $\gamma = 0$ (blue dotted line), and $\alpha = \gamma = 0$ (black dashed line).

$$\mathbf{P}_2(\mathbf{k}) = \frac{\pi}{2} \frac{2\alpha\gamma^2 k_x^4 \left(k_x^2 - 3k_y^2 \right)}{\left[\alpha^2 k^2 + \gamma^2 k_x^2 \left(k_x^2 - 3k_y^2 \right)^2 \right]^{\frac{3}{2}}}. \quad (11)$$

As shown in Fig. 5(c), their integrals $D_{yx}(\mathbf{P}_1)$ and $D_{yx}(\mathbf{P}_2)$ in Eq. (9) are negative and positive, respectively. Both of them increase as the chemical potential decreases. Therefore the Drude-like coefficient $D_{yx}^{\text{C-S}}$, the sum of $D_{yx}(\mathbf{P}_1)$ and $D_{yx}(\mathbf{P}_2)$,

increases with decreasing chemical potential and eventually reverses sign.

Furthermore, we discuss three special cases of Eq. (11) by adjusting parameters α and γ (unit is $-e$):

$$D_{yx}(\mathbf{P}_1) = D_{yx}(\mathbf{P}_2) = 0, \quad \alpha = \gamma = 0$$
$$D_{yx}(\mathbf{P}_1) = D_{yx}(\mathbf{P}_2) = 0, \quad \alpha = 0, \ \gamma \neq 0$$
$$D_{yx}(\mathbf{P}_1) = \alpha m^*/4, \ D_{yx}(\mathbf{P}_2) = 0, \quad \alpha \neq 0, \ \gamma = 0. \quad (12)$$

The corresponding Drude-like coefficients $D_{yx}^{\text{C-S}}$ are shown in Fig. 5(d). In these cases, we note that $D_{yx}^{\text{C-S}}$ is nonzero only if α is nonzero, which reduces to the effect of only the Rashba SOC term. Its analytic expression is a constant, which is only proportional to the Rashba SOC constant α and the effective mass m^*. γ is a parameter quantitatively describing the warping of the hexagon in the vicinity of the Γ point. When γ is also nonzero, $D_{yx}(\mathbf{P}_1)$ is no longer a constant, and $D_{yx}(\mathbf{P}_2)$ have a nonzero value.

The sign reversal of the spin polarization comes from the competition between the intrinsic Rashba SOC and the band warping. For a nonzero k in the FBZ, the band warping effect becomes more significant, as the chemical potential decreases. As shown in Fig. 5(b), due to the band warping effect, the initial concentric circles on the Fermi surface deform into hexagonal rings with a relative rotation angle of $30°$. Simultaneously, the spin texture on the Fermi surface is distorted, which results in the sign reversal of the spin polarization. We separate the Drude-like coefficient $D_{yx}^{\text{C-S}}$ as the sum of $D_{yx}(\mathbf{P}_1)$ and $D_{yx}(\mathbf{P}_2)$. In Fig. 5(c), one can find that the values of $D_{yx}(\mathbf{P}_1)$ and $D_{yx}(\mathbf{P}_2)$ become nonzero as the chemical potential approaches the valence bands at the Γ point, because in the vicinity of the Γ point, the Rashba SOC plays a dominant role in the CISP. It is notable that the values of $D_{yx}(\mathbf{P}_1)$ and $D_{yx}(\mathbf{P}_2)$ are negative and positive initially, the values of both terms tend to increase as the chemical potential decreases, and the sum of the two parts leads to the sign reversal of the spin polarization. In Fig. 5(d), four cases are shown with different combinations of α and γ. We demonstrate that the CISP appears only if the Rashba SOC is nonzero ($\alpha \neq 0$). For the case where the Rashba SOC is included but the band warping effect is absent ($\gamma = 0$), the Drude-like coefficient $D_{yx}^{\text{C-S}}$ remains negative. Furthermore, in the presence of both Rashba SOC and the band warping effect, the Drude-like coefficient $D_{yx}^{\text{C-S}}$ displays a sign reversal as the chemical potential decreases across the critical point.

Then, we discuss the influence of temperature on Drude-like coefficient $D_{yx}^{\text{C-S}}$ in the clean limit. As shown in Fig. 6(a), with the increasing temperature the peak of $D_{yx}^{\text{C-S}}$ tends to be smoothed in the vicinity of $E_{\Gamma m}$. This is a natural result of the broadening of the Fermi-Dirac distribution at finite temperature. Furthermore, the maximum value of $D_{yx}^{\text{C-S}}$ is reduced as the temperature increases, which is consistent with $\mathbf{k} \cdot \mathbf{p}$ Hamiltonian predictions as shown in Fig. 6(b). However, the values of the Drude-like coefficient $D_{yx}^{\text{C-S}}$ are still comparable to the ones of the LAO/STO oxide interface even up to room temperature.

Finally, the disorder effects are taken into account. For a disordered system, $G^{R(A)}$ is the disorder-averaged Green's
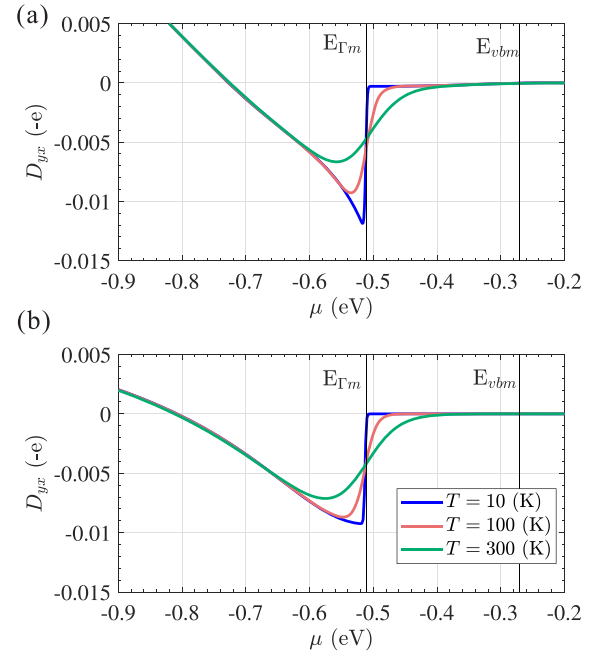

(a)

(b)

FIG. 6. Comparison of the C-S response D_{yx} of the Janus WSSe monolayer obtained by (a) first-principles calculations and (b) the $\mathbf{k} \cdot \mathbf{p}$ Hamiltonian in the clean limit with different temperatures $T = 10$ K (blue lines), $T = 100$ K (red lines), and $T = 300$ K (green lines), respectively.

function and takes the form

$$G^{R(A)} = \frac{1}{\mu - \mathcal{H} \pm i\Gamma}, \quad (13)$$

where $\mathcal{H}$ is the total Hamiltonian written in Eq. (8) and $\Gamma = \hbar/2\tau$. For simplicity, various scattering processes are parametrized with the momentum relaxation time τ phenomenologically. Considering ideal occasions where the scattering processes are weak and rare, one can deal with the transport with a ballistic approximation. We believe that the underlying physics is also similar in the diffusive regime. For randomly distributed short-range impurities, the random potential $V(r)$ with Gaussian correlations $\langle V(r)V(r')\rangle = n_i V_0^2 \delta(r - r')$ is utilized, and the Born approximation is used to obtain $\Gamma = n_i V_0^2 N(\mu)$ without using a vertex correction [57]. The n_i is the impurity density, V_0 is the disorder scattering potential, and $N(\mu)$ is the total DOS at the chemical potential μ as shown in Fig. 2(b).

Figure 7(a) shows the zero-temperature C-S conductivity of the Janus WSSe monolayer, which is calculated at the chemical potential μ with different disorder strengths by using Eq. (1). Compared with the Drude-like coefficient $D_{yx}^{\text{C-S}}$ shown in Fig. 4(a), the C-S conductivity possesses three characteristics. Firstly, as the disorder strength $n_i V_0^2$ increases, the C-S conductivity $\sigma_{yx}^{\text{C-S}}$ decreases monotonically, which is a result of the energy level broadening. Secondly, in the valence band, the K and K' points contribute more to the C-S conductivity, compared with the Drude-like coefficient in the clean-limit case. Finally, it is notable that the sign change of the C-S conductivity occurs at the same chemical potential for different disorder strengths, which is also well consistent with our $\mathbf{k} \cdot \mathbf{p}$
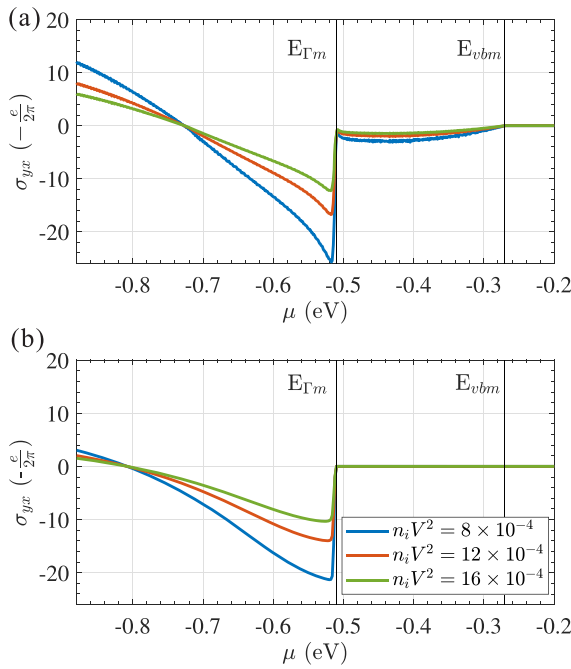
FIG. 7. (a) Comparison of the C-S conductivity $\sigma_{yx}^{\text{C-S}}$ of Janus WSSe monolayer obtained by (a) first-principles calculations and (b) the $\mathbf{k} \cdot \mathbf{p}$ Hamiltonian with different disorder strengths $n_i V_0^2 = 0.8 \times 10^{-3}$ (eV Å)^2 (blue lines), $n_i V_0^2 = 1.2 \times 10^{-3}$ (eV Å)^2 (red lines), and $n_i V_0^2 = 1.6 \times 10^{-3}$ (eV Å)^2 (green lines).

Hamiltonian predictions, as shown in Fig. 7(b). Therefore the sign change is an intrinsic and robust process, due to the interplay between Rashba SOC and hexagonal warping of the energy bands.

The CISP is insensitive to variations of temperature or disorder, yet could be effectively modulated by external strain. In Fig. 8, the effects of biaxial and uniaxial tensile strains on the band structures and CISP are demonstrated. For the biaxial strain, one can find that a direct-indirect band gap transition occurs as the strength of the tensile strain increases. In conduction bands, the CBM remains at the K and K' points. In contrast, in the valence bands, the valleys at the K and K' points descend, while the Γ point ascends. As a consequence, one can find that the critical sign change points of the Janus WSSe monolayer are lifted by approximately 100 meV. The critical sign change points still tend to merge at the same value, since the biaxial tensile strain only lifts the relative energy of the Γ point without changing the anisotropic character of the band dispersion. However, it is notable that the peak of C-S conductivity decreases exponentially as the strength of the biaxial tensile strain increases.

For the uniaxial strain, both the tensile strain applied along the zigzag direction and the tensile strain applied along the armchair direction are studied. From Fig. 8, one can find that both the applied tensile uniaxial strain along the zigzag direction and the applied tensile uniaxial strain along the armchair direction induce the decrease of the C-S conductivity. Compared with the biaxial strain, the peak of the C-S conductivity decreases almost linearly as the strength of the uniaxial
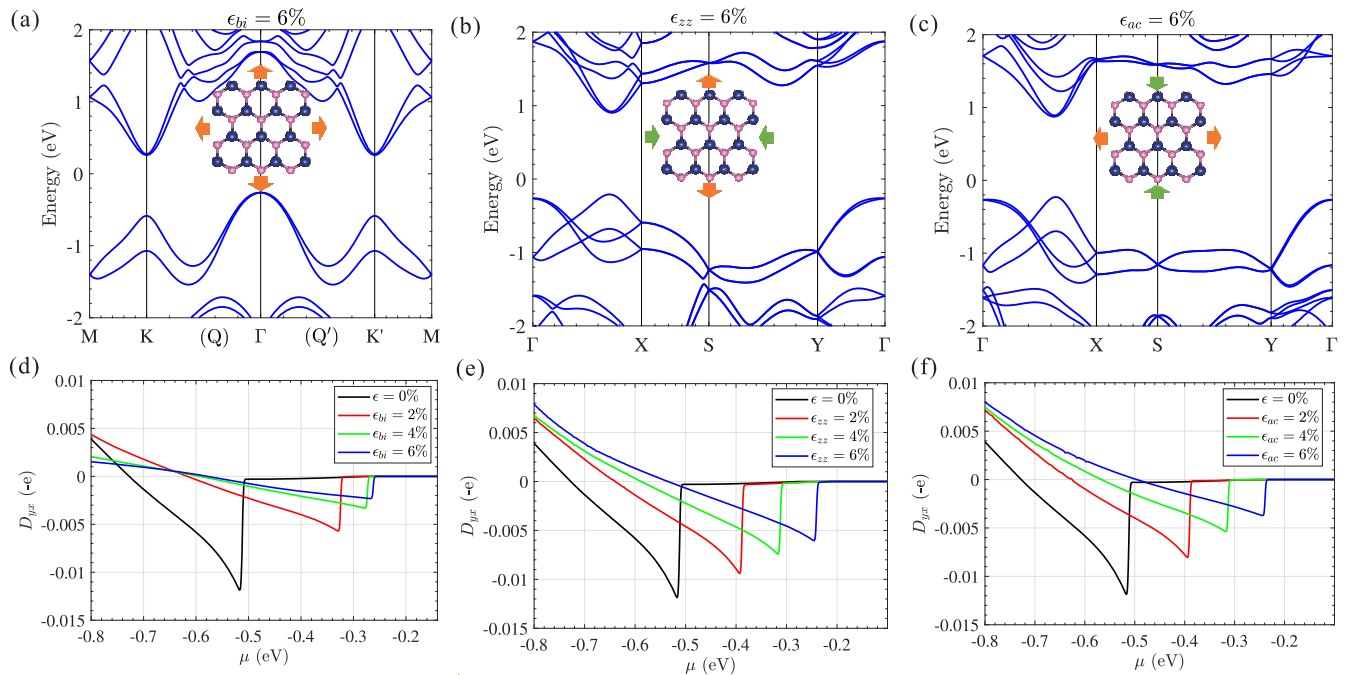

FIG. 8. The upper panels show band structures of the Janus WSSe monolayer under (a) external biaxial tensile strain, (b) external uniaxial tensile strain along the zigzag direction, and (c) external uniaxial tensile strain along the armchair direction. The deformed crystal structures are illustrated as corresponding inset panels, and the deformation is determined as 6% larger with respect to the equilibrium lattice constant. The lower panels show C-S conductivity curves of the Janus WSSe monolayer under various (d) external biaxial tensile strains, (e) external uniaxial tensile strains along the zigzag direction, and (f) external uniaxial tensile strains along the armchair direction. The strengths of the strains are indicated with solid lines of different colors.

strain increases. However, the critical sign change points are shifted. For an applied uniaxial strain as strong as 6%, the critical point is lifted by about 200 meV. The reason can be interpreted by the strain-modulated band structures; from the band structures in Figs. 8(b) and 8(c), one can find out that, even under a uniaxial tensile strain of 6%, the band structures retain their direct-gap characteristic, and the relative positions between the VBM and the Γ point change little. However, the uniaxial strain increases the anisotropy of the band structures and breaks the robustness of the value of the critical sign change point.

It is difficult to tune the chemical potential deep into the sign change point by means of conventional oxide-based transistor gating. Fortunately, utilizing the state-of-the-art techniques of electrostatic gating and intercalation [58], both the effective chemical potential shifting and in-plane strain can be realized simultaneously. For example, ionic gating with lithium-ion-based electrolytes could provide sheet carrier density up to 10^{14} cm^{-2} in monolayer TMD [8], and ionic intercalation causes $\sim$5% uniaxial strain in WTe$_2$ [59]. From this point of view, the sign change and dynamic modulation of the CISP are accessible nowadays.

IV. CONCLUSION

In summary, by performing first-principles calculations, we investigate electronic structures and the CISP of the recently synthesized Janus WSSe monolayer. Because of the vertical mirror symmetry breaking, huge perpendicular built-in polarization as well as large intrinsic Rashba SOC emerge in the Janus WSSe monolayer, and sizable current-spin conductivities are expected both in the conduction bands and in the valence bands. The magnitude of current-spin conductivity is comparable to previously reported values in perovskite oxide interfaces, even at room temperature and in the presence of short-range disorder. Unexpectedly, a robust sign change of the current-spin conductivity is revealed in the valence bands of Janus WSSe. By analyzing the effective Hamiltonian derived from invariant theory, we find that this sign change is a result of the competition between intrinsic Rashba SOC and the hexagonal warping of the valence bands. The CISP in the Janus WSSe monolayer is insensitive to variations of temperature and purity but can be effectively modulated by external biaxial or uniaxial strain. Our analytic and numerical results suggest that the Janus WSSe monolayer not only is an abundant platform to study the interplay between symmetry and degrees of freedom but also could be a promising candidate material to realize flexible two-dimensional spintronics devices.

[1] S. Manzeli, D. Ovchinnikov, D. Pasquier, O. V. Yazyev, and A. Kis, Nat. Rev. Mater. **2**, 17033 (2017).

[2] X. Xu, W. Yao, D. Xiao, and T. F. Heinz, Nat. Phys. **10**, 343 (2014).

[3] K. F. Mak and J. Shan, Nat. Photonics **10**, 216 (2016).

[4] D. Xiao, G.-B. Liu, W. Feng, X. Xu, and W. Yao, Phys. Rev. Lett. **108**, 196802 (2012).

[5] Y. Chen, Y. Huang, W. Lou, Y. Cai, and K. Chang, Phys. Rev. B **102**, 165413 (2020).

[6] F. Liu, J. Zhou, C. Zhu, and Z. Liu, Adv. Funct. Mater. **27**, 1602404 (2017).

[7] H. Yuan, M. S. Bahramy, K. Morimoto, S. Wu, K. Nomura, B.-J. Yang, H. Shimotani, R. Suzuki, M. Toh, C. Kloc, X. Xu, R. Arita, N. Nagaosa, and Y. Iwasa, Nat. Phys. **9**, 563 (2013).

[8] Y. Wang, J. Xiao, H. Zhu, Y. Li, Y. Alsaid, K. Y. Fong, Y. Zhou, S. Wang, W. Shi, Y. Wang, A. Zettl, E. J. Reed, and X. Zhang, Nature (London) **550**, 487 (2017).

[9] J. Zhang, S. Jia, I. Kholmanov, L. Dong, D. Er, W. Chen, H. Guo, Z. Jin, V. B. Shenoy, L. Shi, and J. Lou, ACS Nano **11**, 8192 (2017).

[10] A.-Y. Lu, H. Zhu, J. Xiao, C.-P. Chuu, Y. Han, M.-H. Chiu, C.-C. Cheng, C.-W. Yang, K.-H. Wei, Y. Yang, Y. Wang, D. Sokaras, D. Nordlund, P. Yang, D. A. Muller, M.-Y. Chou, X. Zhang, and L.-J. Li, Nat. Nanotechnol. **12**, 744 (2017).

[11] C. W. Jang, W. J. Lee, J. K. Kim, S. M. Park, S. Kim, and S.-H. Choi, NPG Asia Mater. **14**, 15 (2022).

[12] D. B. Trivedi, G. Turgut, Y. Qin, M. Y. Sayyad, D. Hajra, M. Howell, L. Liu, S. Yang, N. H. Patoary, H. Li, M. M. Petrić, M. Meyer, M. Kremser, M. Barbone, G. Soavi, A. V. Stier, K. Müller, S. Yang, I. S. Esqueda, H. Zhuang *et al.*, Adv. Mater. **32**, 2006320 (2020).

[13] Y.-C. Lin, C. Liu, Y. Yu, E. Zarkadoula, M. Yoon, A. A. Puretzky, L. Liang, X. Kong, Y. Gu, A. Strasser, H. M. Meyer, M. Lorenz, M. F. Chisholm, I. N. Ivanov, C. M. Rouleau, G. Duscher, K. Xiao, and D. B. Geohegan, ACS Nano **14**, 3896 (2020).

[14] Y. Qin, M. Sayyad, A. R.-P. Montblanch, M. S. G. Feuer, D. Dey, M. Blei, R. Sailus, D. M. Kara, Y. Shen, S. Yang, A. S. Botana, M. Atature, and S. Tongay, Adv. Mater. **34**, 2106222 (2022).

[15] Y. Guo, S. Zhou, Y. Bai, and J. Zhao, Appl. Phys. Lett. **110**, 163102 (2017).

[16] D. Er, H. Ye, N. C. Frey, H. Kumar, J. Lou, and V. B. Shenoy, Nano Lett. **18**, 3943 (2018).

[17] S. Liu, J. N. Fry, and H.-P. Cheng, Phys. Rev. Mater. **5**, 064007 (2021).

[18] T. Zheng, Y.-C. Lin, Y. Yu, P. Valencia-Acuna, A. A. Puretzky, R. Torsi, C. Liu, I. N. Ivanov, G. Duscher, D. B. Geohegan, Z. Ni, K. Xiao, and H. Zhao, Nano Lett. **21**, 931 (2021).

[19] Q.-F. Yao, J. Cai, W.-Y. Tong, S.-J. Gong, J.-Q. Wang, X. Wan, C.-G. Duan, and J. H. Chu, Phys. Rev. B **95**, 165401 (2017).

[20] S. B. Yu, M. Zhou, D. Zhang, and K. Chang, Phys. Rev. B **104**, 075435 (2021).

[21] I. Žutić, J. Fabian, and S. Das Sarma, Rev. Mod. Phys. **76**, 323 (2004).

[22] D. D. Awschalom and M. E. Flatté, Nat. Phys. **3**, 153 (2007).

[23] A. Fert, Rev. Mod. Phys. **80**, 1517 (2008).

[24] J. Sinova, S. O. Valenzuela, J. Wunderlich, C. H. Back, and T. Jungwirth, Rev. Mod. Phys. **87**, 1213 (2015).

[25] A. Manchon, H. C. Koo, J. Nitta, S. M. Frolov, and R. A. Duine, Nat. Mater. **14**, 871 (2015).

[26] A. Soumyanarayanan, N. Reyren, A. Fert, and C. Panagopoulos, Nature (London) **539**, 509 (2016).

[27] M. Lindemann, G. Xu, T. Pusch, R. Michalzik, M. R. Hofmann, I. Žutić, and N. C. Gerhardt, Nature (London) **568**, 212 (2019).

[28] W. Yang, K. Chang, and S.-C. Zhang, Phys. Rev. Lett. **100**, 056602 (2008).

[29] V. M. Edelstein, Solid State Commun. **73**, 233 (1990).

[30] A. G. Aronov and Y. B. Lyanda-Geller, JETP Lett. **50**, 431 (1989).

[31] A. G. Aronov, Y. B. Lyanda-Geller, and G. E. Pikus, Sov. Phys. JETP **73**, 537 (1991).

[32] E. L. Ivchenko, Y. B. Lyanda-Geller, and G. E. Pikus, JETP Lett. **50**, 175 (1989).

[33] E. L. Ivchenko and S. Ganichev, *Spin Physics in Semiconductors*, edited by M. I. Dyakonov (Springer, New York, 2008).

[34] T. S. Ghiasi, A. A. Kaverzin, P. J. Blah, and B. J. van Wees, Nano Lett. **19**, 5959 (2019).

[35] C. H. Li, O. M. J. van 't Erve, S. Rajput, L. Li, and B. T. Jonker, Nat. Commun. **7**, 13518 (2016).

[36] C. H. Li, O. M. J. van 't Erve, J. T. Robinson, Y. Liu, L. Li, and B. T. Jonker, Nat. Nanotechnol. **9**, 218 (2014).

[37] M. Zhou, S. B. Yu, W. Yang, W. k. Lou, F. Cheng, D. Zhang, and K. Chang, Phys. Rev. B **100**, 245409 (2019).

[38] J. Shi, P. Zhang, D. Xiao, and Q. Niu, Phys. Rev. Lett. **96**, 076604 (2006).

[39] K. Shen, G. Vignale, and R. Raimondi, Phys. Rev. Lett. **112**, 096601 (2014).

[40] M. Zhou, D. Zhang, S. B. Yu, Z. Huang, Y. Chen, W. Yang, and K. Chang, Phys. Rev. B **99**, 155402 (2019).

[41] G. L. Bir and G. E. Pikus, *Symmetry and Strain-Induced Effects in Semiconductors* (Wiley/Halsted, New York, 1974).

[42] M. S. Dresselhaus, G. Dresselhaus, and A. Jorio, *Group Theory: Application to the Physics of Condensed Matter* (Springer, Berlin, 2007).

[43] M. Zhou, R. Zhang, J. Sun, W.-K. Lou, D. Zhang, W. Yang, and K. Chang, Phys. Rev. B **96**, 155430 (2017).

[44] L. Fu, Phys. Rev. Lett. **103**, 266801 (2009).

[45] D. A. Papaconstantopoulos and M. J. Mehl, J. Phys.: Condens. Matter **15**, R413 (2003).

[46] W. M. C. Foulkes and R. Haydock, Phys. Rev. B **39**, 12520 (1989).

[47] G. Pizzi, V. Vitale, R. Arita, S. Blügel, F. Freimuth, G. Géranton, M. Gibertini, D. Gresch, C. Johnson, T. Koretsune, J. Ibañez-Azpiroz, H. Lee, J.-M. Lihm, D. Marchand, A. Marrazzo, Y. Mokrousov, J. I. Mustafa, Y. Nohara, Y. Nomura, L. Paulatto *et al.*, J. Phys.: Condens. Matter **32**, 165902 (2020).

[48] N. Marzari and D. Vanderbilt, Phys. Rev. B **56**, 12847 (1997).

[49] I. Souza, N. Marzari, and D. Vanderbilt, Phys. Rev. B **65**, 035109 (2001).

[50] G. Kresse and J. Hafner, Phys. Rev. B **49**, 14251 (1994).

[51] G. Kresse and J. Furthmüller, Phys. Rev. B **54**, 11169 (1996).

[52] W. Kohn and L. J. Sham, Phys. Rev. **140**, A1133 (1965).

[53] P. Hohenberg and W. Kohn, Phys. Rev. **136**, B864 (1964).

[54] P. E. Blöchl, Phys. Rev. B **50**, 17953 (1994).

[55] J. P. Perdew, K. Burke, and M. Ernzerhof, Phys. Rev. Lett. **77**, 3865 (1996).

[56] G. Seibold, S. Caprara, M. Grilli, and R. Raimondi, Phys. Rev. Lett. **119**, 256801 (2017).

[57] A. Dyrdał and J. Barnaś, Phys. Rev. B **92**, 165404 (2015).

[58] Y. Wu, D. Li, C.-L. Wu, H. Y. Hwang, and Y. Cui, Nat. Rev. Mater. **8**, 41 (2023).

[59] P. K. Muscher, D. A. Rehn, A. Sood, K. Lim, D. Luo, X. Shen, M. Zajac, F. Lu, A. Mehta, Y. Li, X. Wang, E. J. Reed, W. C. Chueh, and A. M. Lindenberg, Adv. Mater. **33**, 2101875 (2021).